J. Fluid Mech. (1988), *vol.* 192, *pp.* 219–247
Printed in Great Britain

Surface waves due to resonant horizontal oscillation

By M. FUNAKOSHI AND S. INOUE
Research Institute for Applied Mechanics, Kyushu University, Kasuga, Fukuoka 816, Japan

(Received 31 August 1987 and in revised form 11 November 1987)

Experiments on surface waves were made using a cylindrical container oscillated horizontally with the period T close to that associated with the two known degenerate modes. Outside a certain region in the (T, x_0)-plane, where x_0 is the amplitude of the forcing displacement, surface waves exhibit either of the two kinds of regular motions whose amplitudes are constant. Within this region, however, the wave amplitude slowly changes, expressing the irregular or periodic motion of surface waves. In order to analyse these motions in detail, the slow evolution of four variables associated with the amplitudes and phases of the two modes is computed from the free-surface displacement at two measuring points. It is shown that the most common attractor corresponding to the irregular wave motion is the strange attractor with a positive maximum Liapunov exponent and a correlation dimension of 2.1–2.4. Furthermore, another kind of chaotic attractor and a few periodic orbits are found in a small parametric region. The route to chaos associated with period-doubling bifurcation is also observed. The above experimental results are compared with the solutions to weakly nonlinear evolution equations derived by Miles. We find that the equations can explain well many of the experimental results on regular and irregular wave motions. In particular, the most common chaotic attractors both in the experiments and in the theory have similar shapes in a phase space, and also yield similar values for maximum Liapunov exponents and correlation dimensions.

1. Introduction

Irregular motions are commonly found in fluid systems. There has been attempts to understand some of them from the standpoint of the chaos in systems having only a few degrees of freedom. Two famous examples are Rayleigh–Bénard convection and Taylor–Couette flow.

Besides these systems, surface waves in a closed basin are known to evolve irregularly under appropriate regular resonant oscillation of the container. Ciliberto & Gollub (1985) experimentally investigated the evolution of surface waves due to vertical oscillation of a cylindrical container at frequencies close to those of the two nearly degenerate modes. They found a slowly evolving chaotic or periodic motion in a certain region of amplitude and frequency of the forcing. The attractor corresponding to the chaotic motion was shown to have a dimension close to 2.2 and at least one positive Liapunov exponent. Furthermore, they observed the route to chaos associated with period-doubling bifurcations. Gollub & Meyer (1983) examined the evolution of a single mode due to vertical oscillation. Keolian *et al.* (1981) studied surface waves due to vertical oscillation in thin annular troughs. Both experiments also found period-doubling bifurcations and chaotic motions.

Hutton (1963) did experiments on surface waves due to harmonic horizontal

oscillation in a circular cylinder. He chose the driving frequency in the neighbourhood of the natural frequency of the two degenerate modes, whose free-surface displacements η can be written as

$$\eta \propto J_1(kr)\begin{cases}\cos\theta \\ \sin\theta\end{cases}, \tag{1.1}$$

where r and θ are plane polar coordinates on which the axis of oscillation is $\theta = 0$ and π. The value of k is chosen so that ka is the smallest positive zero of J_1'. Here a is the radius of the cylinder. In this experiment he found two regular wave motions in certain regions of amplitude and frequency of the forcing. The first is a planar oscillation in which the points of largest amplitude always lie on the axis of oscillation. The second is a regular rotational motion in which the point of largest free-surface displacement rotates regularly along the wall. He found the regions where these motions can be observed, although the boundary of the regular rotational motion region is not definite. He furthermore found that the surface waves evolve irregularly in a certain parametric region. He did not study this behaviour quantitatively however.

Miles (1976) proposed a weakly nonlinear theory for surface waves in a cylindrical container. According to this theory, he derived evolution equations for horizontal or vertical resonant oscillation of a cylindrical container (Miles 1984*a*, *b*). Miles (1984*b*, *c*) then examined the properties of the solutions to these evolution equations for horizontal oscillation, which is similar to the configuration of Hutton's experiments. He found two kinds of fixed points corresponding to the two regular wave motions in the experiments. He also obtained limit cycles and chaotic attractors expressing periodic and irregular modulations of the amplitude of free-surface displacement, respectively.

In this paper, we first describe the evolution of surface waves in an experiment similar to that of Hutton. Our main aim is to examine the irregular wave motion in detail from the standpoint of the chaos in systems having only a few degrees of freedom. We describe the experimental configuration in §2. The results of the experiment are given in §3. We accurately determined the regions in the (T, x_0)-plane where planar oscillations or regular rotational motions can be observed. Here T is the period of the oscillation, and x_0 its amplitude. Outside these regions, the wave amplitude at any point slowly changes, expressing the irregular or periodic motion of surface waves. In order to analyse these motions in detail, the slow evolution of four variables associated with the amplitudes and phases of the two modes given in (1.1) was computed from the free-surface displacement at two measuring points. Consequently, it is shown that the most common attractor corresponding to the irregular wave motion is the strange attractor with a positive maximum Liapunov exponent and a correlation dimension of 2.1–2.4. Furthermore, another kind of chaotic attractor and a few periodic orbits are found in a small parametric region. The route to chaos associated with period-doubling bifurcation is also observed.

Next, the relevant evolution equations derived by Miles, given in §4, were solved numerically to compare their solutions with the above experimental results. After describing in §5 the properties of some of the solutions, some comparisons with the experimental results are made in §6. Consequently, we find that the evolution equations can explain well many of the experimental results on regular and irregular wave motions. That is, the regions in the (T, x_0)-plane where regular planar oscillations or regular rotational motions are experimentally observed almost coincide with the regions where stable fixed points corresponding to these wave

motions exist. Furthermore, a few irregular or periodic wave motions are experimentally observed, approximately in the same parametric region where the equations point to chaotic attractors or limit cycles. The attractor similar to the most common chaotic attractor found in the experiments is commonly found as the solutions to the equations in the same parametric region. The correlation dimensions and the maximum Liapunov exponents of these two attractors yield similar values. Moreover, the transition to chaos associated with the period-doubling bifurcation is found both in the experiments and in the theory. Some discrepancies, however, remain. For example, many of the limit cycles of the evolution equations are not stably observed in the experiments. Next, we attempt to explain the reason for the discrepancies, taking into consideration the effect of the unavoidable variation of T in the experiments, and the assumptions made in the theory.

Finally, the relevance of the experimental results to those of the experiments by Ciliberto & Gollub (1985) is discussed in §7.

2. Experimental configuration

In the experiments, a cylindrical tank of radius $a = 9.24$ cm, partially filled with water to a depth $d = 14.1$ cm, is oscillated sinusoidally using a mechanical driving system, shown in figure 1, consisting of a crank mechanism connected to a servomotor. A bearing guide restricts the oscillation to a specified horizontal direction. The water temperature is kept at 18.1 ± 0.1 °C, so as to make thermal variations in viscosity insignificant.

The oscillation period T is measured by transmitting the pulse from a magnetic-type detector to a frequency counter. The variation of T is at most 0.035%. The amplitude of the displacement of the tank, x_0, is adjusted by changing the stroke of the crank mechanism. The oscillation can be regarded as nearly sinusoidal, since the energy of the higher harmonics is only 0.19% of that of the primary wave.

Free-surface displacement was measured at two points M_1 $[(r, \theta) = (0.87a, 0)]$ and M_2 $[(r, \theta) = (0.87a, \frac{1}{2}\pi)]$ using a capacity-type wave-height meter. These free-surface displacements as well as the displacement of the tank are recorded simultaneously in a data recorder.

The period associated with the modes given in (1.1) can be written as

$$T_0 = \frac{2\pi}{(kg \tanh kd)^{\frac{1}{2}}}, \tag{2.1}$$

where g is the gravitational acceleration and $ak = 1.8412$. The value T_0 is 0.4513 s for the above values of a and d. Hereafter, we use

$$T_{\mathrm{r}} = \frac{T - T_0}{T_0} \tag{2.2}$$

instead of T. The experiments were done for $-0.125 \leqslant T_{\mathrm{r}} \leqslant 0.075$ and $x_0 \leqslant 0.1$ cm.

The behaviour of surface waves was usually examined by slowly increasing or decreasing T_{r} with a fixed x_0. In order to exclude transient effects, we made the observation or recording of surface waves after waiting at least 20 min., keeping T_{r} fixed. The free-surface displacements at two points and the tank displacement were recorded for 40 min. (about $5000T$) for $x_0 = 0.05$ cm only.

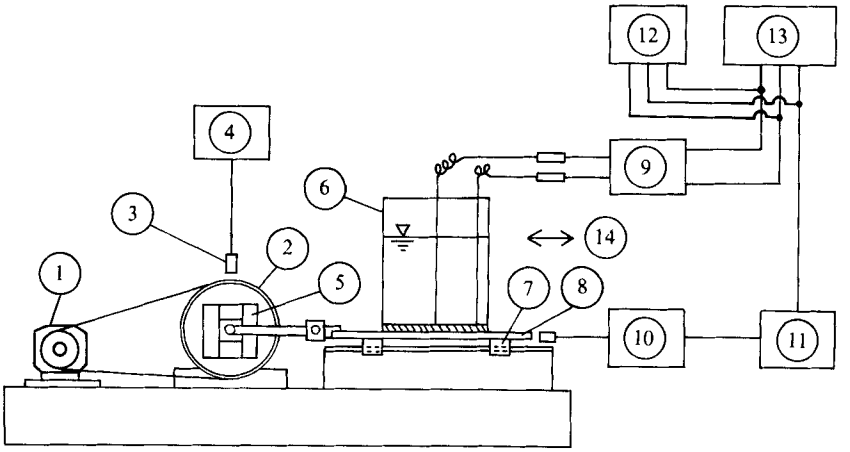

FIGURE 1. Schematic diagram of the apparatus. 1. AC 400W servomotor; 2. pulley; 3. magnetic-type detector; 4. frequency counter; 5. crank mechanism; 6. water tank; 7. bearing guide; 8. oscillating table; 9. wave-height meter; 10. displacement transducer; 11. linearizer; 12. data recorder; 13. pen recorder; 14. the direction of oscillation.

3. Experimental results

3.1. *Phase diagram*

Figure 2 shows the behaviour of surface waves due to horizontal oscillation with displacement.

$$x = x_0 \cos\frac{2\pi}{T}t. \tag{3.1}$$

Here T_r, defined in (2.2), is used as an abscissa in place of T. If $|T_r|$ is sufficiently large, that is on the left of the line L_1 or on the right of the line L_4 in figure 2, a regular planar oscillation is observed, regardless of initial states. The contour lines of free-surface displacement in this motion are always symmetric about the axis of oscillation, and thus the points of largest amplitude are always on this axis.

On the other hand, if $|T_r|$ is sufficiently small, that is in the region between the lines L_2 and L_3, a regular rotational motion is observed, regardless of initial states. In this motion, the point of largest free-surface displacement rotates regularly along the wall. Both clockwise and anticlockwise rotations are possible because of the symmetry of the system about the axis of oscillation. The initial condition determines the direction of the rotation.

In the region between the lines L_1 and L_2, either the regular planar oscillation or the regular rotational motion can be observed, depending on the initial condition. That is, the planar oscillation appears when we suddenly start the forcing with (T_r, x_0) in this region or when T_r is increased slowly from the region on the left of the line L_1 with fixed x_0. In contrast to this, the regular rotational motion continues when T_r is decreased slowly from the region between the lines L_2 and L_3 with fixed x_0.

In the case of the above two regular motions, the amplitudes of the free-surface displacements at any point do not change with time. In the region between the lines L_3 and L_4 in figure 2, however, the amplitudes change irregularly or periodically, and the timescale of the change is much larger than the period of the forcing. A detailed analysis of this motion was made mainly for $x_0 = 0.05$ cm. The results will be shown in the following subsections.

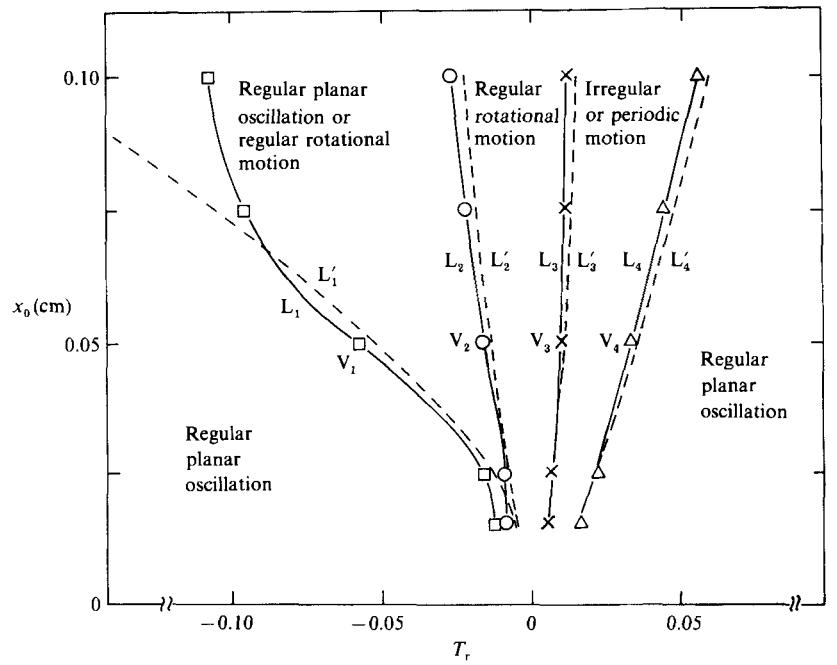

FIGURE 2. Phase diagram as a function of the period relative to the resonant period T_r and the amplitude x_0 of the forcing. The boundaries of the regions for several wave motions in the experiments are expressed by solid lines connecting the measured points denoted by the symbols. Broken lines denote the boundaries where the number of stable fixed points of (4.5) changes.

The classification of wave motions was not done for $x_0 < 0.016$ cm, since the free-surface displacements are too small for direct observation or for analysis of recorded data. Breaking of waves seems not to occur for $x_0 \leqslant 0.05$ cm, whereas small breaking may occur in the irregular wave motion for $x_0 \geqslant 0.075$ cm.

The phase diagram figure 2 is consistent with Hutton's experimental results on the regular planar oscillation.

3.2. *Irregular or periodic wave motions*

When x_0 is fixed at 0.05 cm and T_r is increased slowly from the values between those at V_2 and V_3 in figure 2 and beyond, the following changes in surface-wave motion occur. For T_r less than 0.0063, that is on the left of V_3, we observe the regular rotational motion, as mentioned in §3.1. When T_r increases beyond this value, the motion becomes unstable and a slow modulation of the amplitudes is observed. Until T_r reaches 0.0102, the point of largest free-surface displacement continues to rotate in one direction, although the speed of the rotation varies slowly with time. The evolution of wave amplitudes in this unidirectionally rotating motion is periodic for $0.0063 < T_r < 0.0093$, but is irregular for $0.0093 < T_r < 0.0102$.

When T_r increases beyond 0.0102, we can observe a bidirectionally rotating motion, in which the direction of the rotation changes irregularly. This motion is associated with irregular slow evolution of both the wave amplitudes and the speed of the rotation. In the range where $0.0102 < T_r < 0.0133$, both the unidirectionally and the bidirectionally rotating irregular motions can be observed. The two motions appear alternately at long irregular time intervals. The larger T_r is, the smaller the ratio of the time interval for the unidirectionally rotating motion. In the relatively

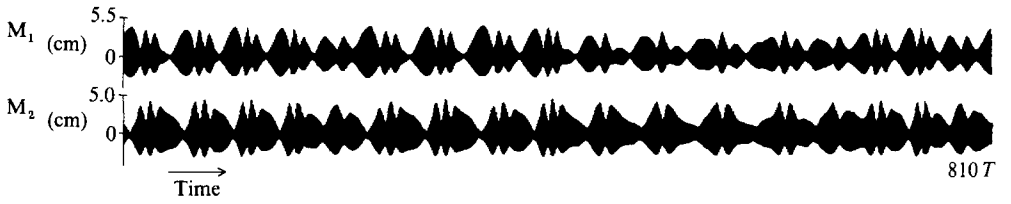

FIGURE 3. Time evolution of the amplitudes of free-surface displacements at two measuring points: M_1 at $(r, \theta) = (0.87a, 0)$ and M_2 at $(r, \theta) = (0.87a, \frac{1}{2}\pi)$: $x_0 = 0.05$ cm and $T_r = 0.0196$. The primary wave of period T is not appreciable in this figure.

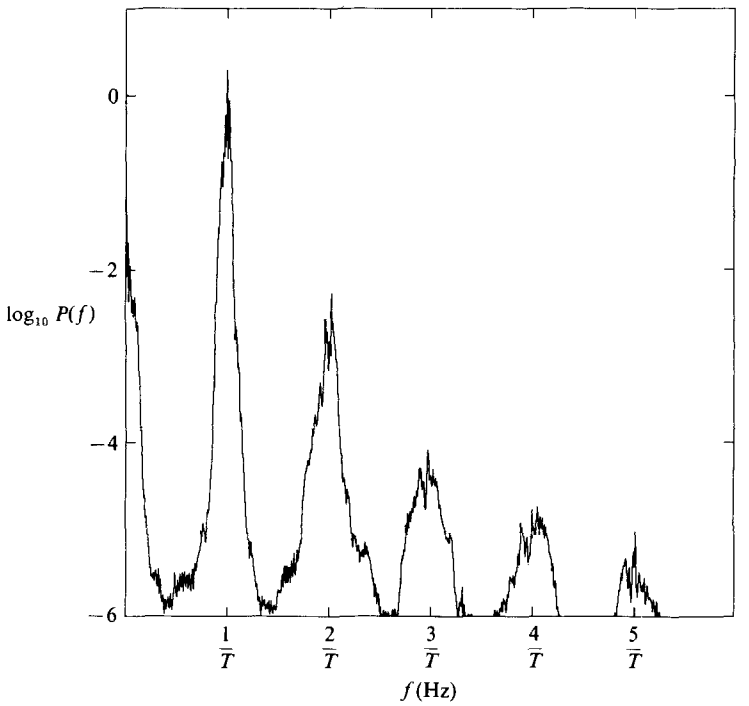

FIGURE 4. Power spectrum shown on a logarithmic scale computed from the free-surface displacement at M_1: $x_0 = 0.05$ cm and $T_r = 0.0196$. There are fairly narrow peaks with frequencies f around $1/T$, $2/T$, ...

wide range where $0.0133 < T_r < 0.0326$, only the irregular bidirectionally rotating motion is observed. One example of this motion is shown in figure 3, where the evolution of the amplitudes of free-surface displacements at two measuring points M_1 and M_2 is given. Note that the primary wave of the period T is not shown explicitly. Figure 4 represents the power spectrum computed from the free-surface displacement at M_1 shown in figure 3. Reflecting the slow modulation, there are fairly narrow peaks with frequencies f around $1/T$, $2/T$, ...

For T_r within the narrow region where $0.0326 < T_r < 0.0332$, we observe an approximately periodic wave motion, in which the amplitudes of free-surface displacements vary almost periodically and the direction of the rotation changes almost regularly. If T_r increases a little more, to 0.0332, which corresponds to V_4 in figure 2, the regular planar oscillation is observed.

On the other hand, when T_r is slowly reduced from the value corresponding to the regular planar oscillation, this motion continues until T_r reaches 0.0290, where

the irregular bidirectionally rotating motion emerges, but the approximately periodic wave motion is not found. Therefore, in the narrow region where $0.0290 < T_r < 0.0332$, the wave motion depends on the initial condition. For smaller decreasing values of T_r, the wave motion is approximately the same as that obtained by the slow increase of T_r.

3.3. *Analysis based on four variables associated with two relevant modes*

In order to examine quantitatively the various wave motions introduced in the preceding subsections, the following analysis is made for $x_0 = 0.05$ cm and $0.005 \leqslant T_r \leqslant 0.034$. First, since T_r is close to zero, we assume that the free-surface displacement η can be expressed as

$$\eta = [(p_1 \cos\omega t + q_1 \sin\omega t)\cos\theta + (p_2 \cos\omega t + q_2 \sin\omega t)\sin\theta]\frac{J_1(kr)}{J_1(0.87ak)} + \hat{N}(t, r, \theta), \tag{3.2}$$

where r and θ are plane polar coordinates on which the axis of oscillation is $\theta = 0$ and π, and $\omega = 2\pi/T$ and $ak = 1.8412$. The four variables p_1, q_1, p_2 and q_2 are assumed to evolve with a timescale much larger than T.

Since in our system there is no other mode whose natural period is close to T_0, the contribution of any other mode may be neglected. As illustrated in figure 4, the remaining term $\hat{N}(t, r, \theta)$ consists mainly of the components that evolve with periods close to $\frac{1}{2}T$, $\frac{1}{3}T$, ... Their energy is considerably smaller than that of the primary wave for (T_r, x_0) in the above parametric region. Moreover, for these (T_r, x_0) the assumption of slow variation of p_1, q_1, p_2 and q_2 is certainly valid, as illustrated in figure 3. Therefore, the evolution of surface waves may approximately be expressed by the slow variation of the four variables.

The values of p_1, q_1, p_2 and q_2 were computed for each period of time with interval T from the free-surface displacements at two points $\mathbf{M}_1$ and $\mathbf{M}_2$, by integrating over the time T the above data multiplied by $\cos\omega t$ or $\sin\omega t$. The evolution of wave motion is approximately represented by the trajectory of $\boldsymbol{p} = (p_1, q_1, p_2, q_2)$ in four-dimensional phase space. Here we should note that if a trajectory $(p_1(t), q_1(t), p_2(t), q_2(t))$ is observed, then the trajectory $(p_1(t), q_1(t), -p_2(t), -q_2(t))$ is also observable. This is due to the symmetry of the system with respect to the axis of oscillation.

The $\boldsymbol{p}$ for the regular planar oscillation or the regular rotational motion always has a constant value; here p_2 and q_2 are zero only for the planar case. Figure 5 shows the T_r-dependence of $(p_1^2 + q_1^2)^{\frac{1}{2}}$, which approximates the amplitude of the free-surface displacement at $\mathbf{M}_1$. The amplitude for the regular planar oscillation increases as T_r approaches zero. The amplitude for the regular rotational motion is larger than that for the regular planar oscillation, and increases as T_r decreases. Hutton's experiment gives similar results. For T_r between $\mathbf{V}_3$ and $\mathbf{V}_4$ in figure 5, the amplitude varies in time, and only its maximum value is shown. The maximum amplitude for the irregular bidirectionally rotating motion, denoted by triangles, is larger than that for any regular wave motions, and increases with T_r. The maximum amplitude for the unidirectionally rotating motion, denoted by squares, increases rapidly with T_r. Then the transition to the irregular motion (especially to the bidirectionally rotating motion) can be said to give rise to the rapid increase in the maximum wave amplitude.

Next, we show the attractors, represented by the trajectories of $\boldsymbol{p}$ in the phase space, for several kinds of wave motions. To express the attractors, we use the projections of the trajectories to one or four two-dimensional subspaces. Figures 6

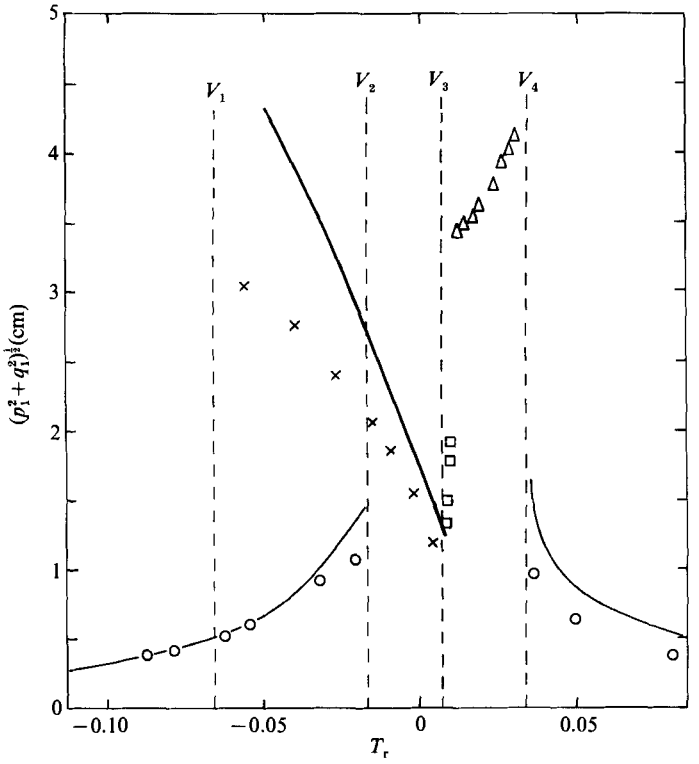

FIGURE 5. The T_r-dependence of $(p_1^2+q_1^2)^{\frac{1}{2}}$, which approximates the amplitude of free-surface displacement at M_1: $x_0 = 0.05$ cm. Circles and crosses denote the experimental values for the regular planar oscillation and the regular rotational motion, respectively. Triangles and squares denote the maximum values of $(p_1^2+q_1^2)^{\frac{1}{2}}$ for the irregular bidirectionally and unidirectionally rotating motions, respectively. The values for the fixed points of (4.5) corresponding to the regular planar oscillation and the regular rotational motion are expressed by thin and bold solid lines, respectively. Broken lines denote the boundaries of the regions for several wave motions in the experiments.

and 7(*a*) show the attractors throughout the transition from the regular rotational motion to the irregular unidirectionally rotating motion. Hopf bifurcation occurs at $T_r = 0.0063$ and then limit cycles are observed for $0.0063 < T_r < 0.0090$ (figure 6*b*, *c*). Afterwards period-doubling bifurcation occurs at $T_r = 0.0090$, as shown in figure 6(*d*). For $0.0093 < T_r < 0.0102$, we obtain the chaotic attractor shown in figure 7(*a*). Although the successive period-doubling bifurcations are predicted theoretically as one of the routes to chaos for $0.0090 < T_r < 0.0093$, the second period-doubling bifurcation was not found, probably because our experiments were insufficiently accurate.

An example of the attractor for irregular bidirectionally rotating motion is shown in figure 7(*b*). Although such attractors are commonly observed for $0.0133 < T_r < 0.0326$, the uneven chaotic attractors illustrated in figure 8(*c*) are also found occasionally in this region. In the case of the latter attractors, the points in a certain subset are visited more frequently than those outside it. No systematic relation was found about the values of T_r for which uneven chaotic attractors are observed. Although no stable periodic motion was observed in this region, we found some interesting wave motions which continue only for a finite time. Figures 8(*a*) and 8(*b*)

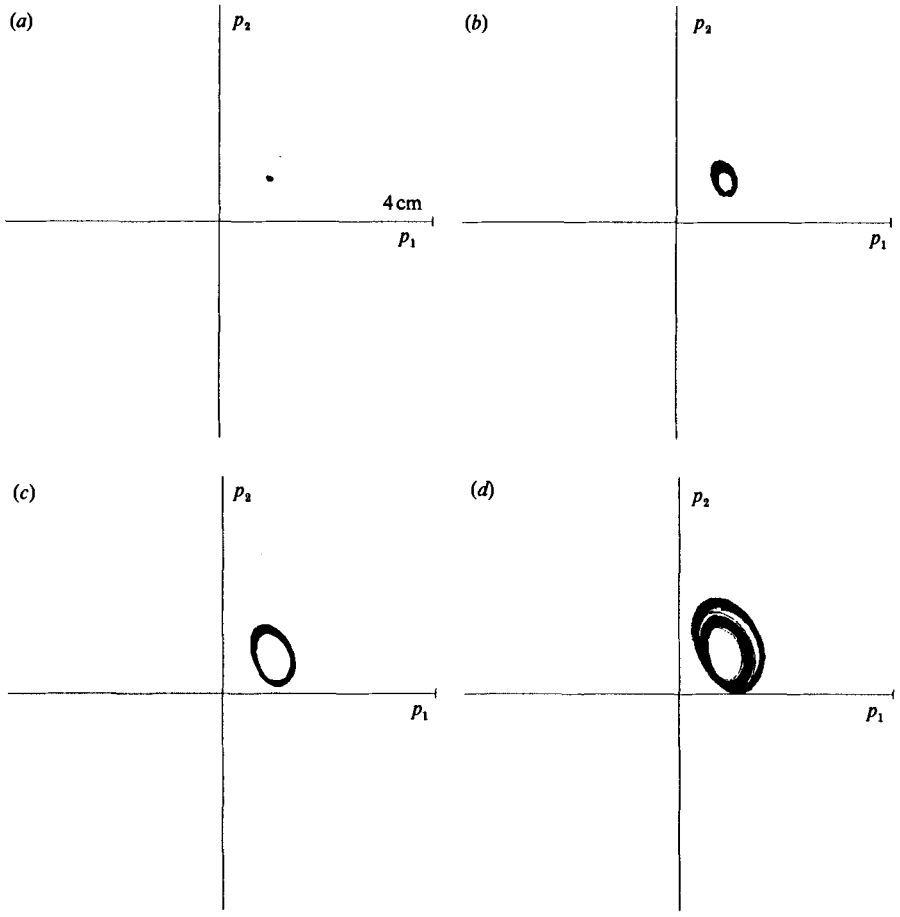

FIGURE 6. Attractors for the unidirectionally rotating motion expressed by projecting onto the (p_1, p_2)-plane: $x_0 = 0.05$ cm. (*a*) $T_r = 0.0059$, regular rotational motion; (*b*) $T_r = 0.0065$; (*c*) $T_r = 0.0076$; (*d*) $T_r = 0.0090$. Hopf bifurcation and period-doubling bifurcation are shown.

show the unstable approximately periodic wave motions observed for $1100T$ and $1500T$ respectively. Figure 9 also shows this kind of wave motion, but with a life span much shorter than that of figure 8(*a*, *b*). The trajectories in figure 9(*a*, *b*) are approximately invariant under the transformation $(p_1, q_1, p_2, q_2) \to (p_1, q_1, -p_2, -q_2)$, while that in figure 9(*c*) is not invariant under this transformation. The above results on the uneven chaotic attractors and the unstable approximately periodic wave motions suggest that windows for periodic motions may be found even in the region where $0.0133 < T_r < 0.0326$ if a much more accurate experimental apparatus is used. This is an unresolved problem.

The attractor for the approximately periodic bidirectionally rotating motion is shown in figure 7(*c*). This is not invariant under the above transformation. Since the 'width' of the band in this attractor varies along the orbit, it is suggested that this band structure does not express the noise itself, although it may be induced by the noise.

In order to examine the properties of attractors quantitatively, we first compute the power spectrum from the evolution of

$$E = \tfrac{1}{2}(p_1^2 + q_1^2 + p_2^2 + q_2^2). \tag{3.3}$$

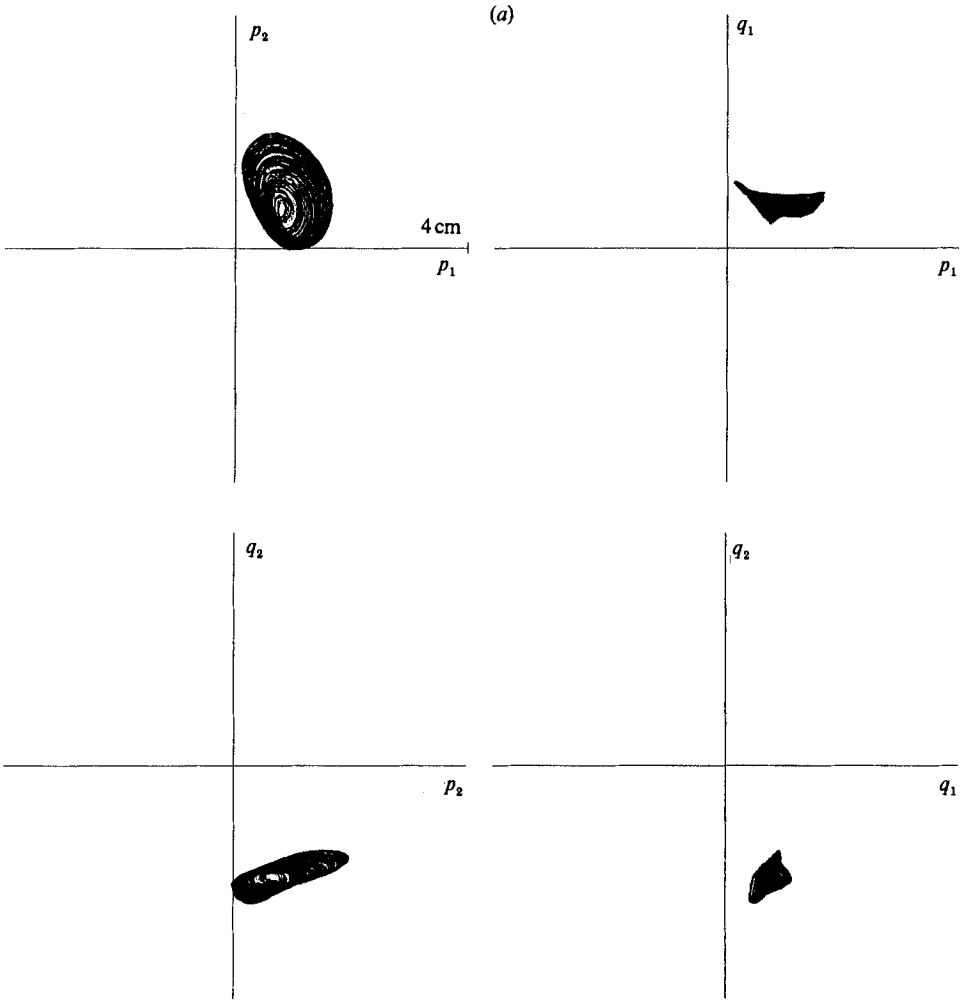

FIGURE 7(*a*). For caption see page 230.

which is the measure of wave energy. The results are shown on a logarithmic scale in figure 10. Here zero-frequency components of the power spectra are eliminated. The power spectra for the periodic orbit shown in figure 6(*c*) and the approximately periodic orbit shown in figure 7(*c*) are shown in figures 10(*a*) and 10(*d*). Both of them contain only relatively sharp peaks. The periods of the fundamental components are $34T$ and $55T$ in figures 10(*a*) and 10(*d*). On the other hand, the irregular wave motions shown in figure 7(*a*, *b*) exhibit the power spectra shown in figure 10(*b*, *c*), where broadband components as well as some peaks are certainly found. The periods associated with large peaks are around $50T$ in these spectra. Therefore, it can be said that if T_r is in the region of irregular or periodic wave motions, then the evolution of E defined in (3.3) is certainly much slower than that of the primary wave.

3.4. *Correlation dimension and Liapunov exponent*

To characterize attractors, their dimensions are very important factors. Among various kinds of dimensions we use the correlation dimension suggested by

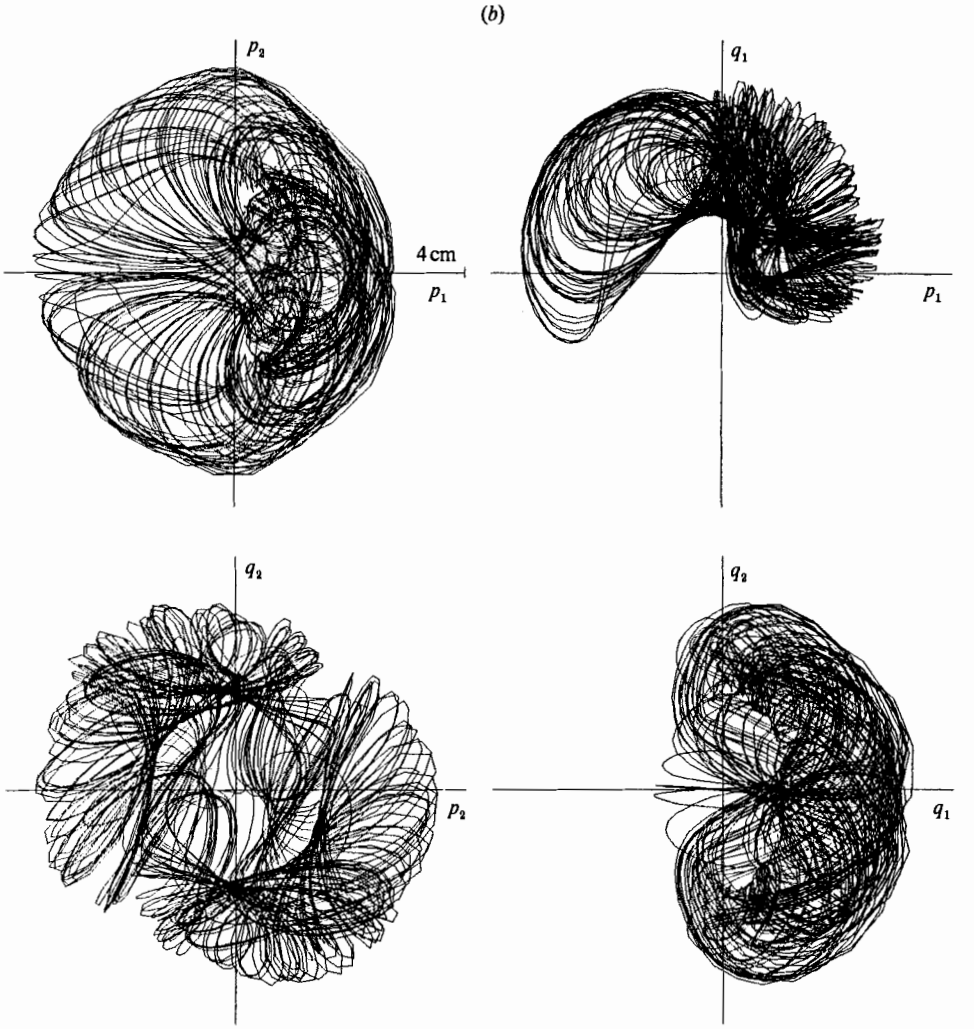

FIGURE 7(*b*). For caption see page 230.

Grassberger & Procaccia (1983). In order to obtain this dimension, we first compute the correlation function

$$C(R) = \frac{2}{N(N-1)} \sum_{\substack{i,j=1 \\ i \neq j}}^{N} H(R - |\boldsymbol{p}_i - \boldsymbol{p}_j|), \tag{3.4}$$

from the data of

$$\boldsymbol{p}_n = (p_1(nT), q_1(nT), p_2(nT), q_2(nT)) \quad (n = 1, 2, \ldots, N), \tag{3.5}$$

where $H(R)$ is the step function

$$H(R) = \begin{cases} 1, & \text{for } R \geqslant 0, \\ 0, & \text{for } R < 0, \end{cases} \tag{3.6}$$

and Euclidean distance is used as the distance between two vectors. Then, we can usually find the linear dependence of $\log C(R)$ on $\log R$ in a certain region where $R_{\min} < R < R_{\max}$. The correlation dimension ν is computed from the gradient of

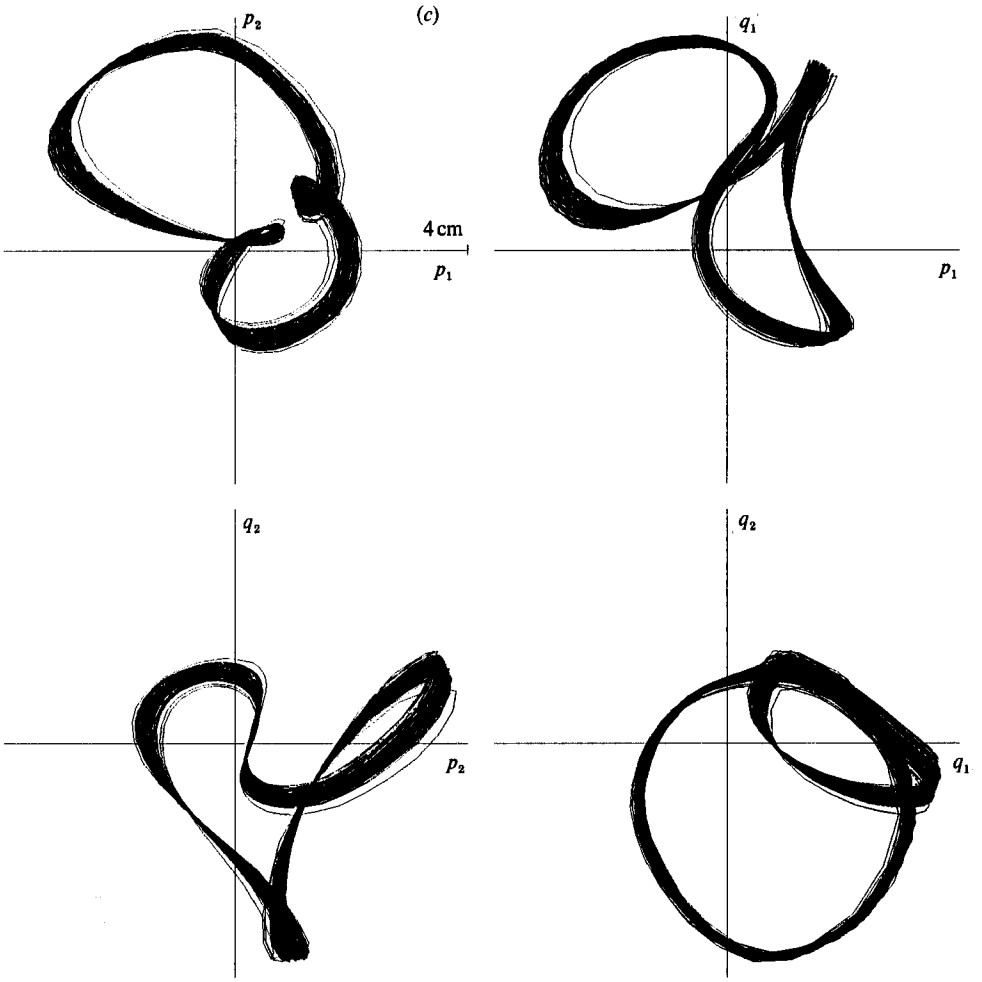

FIGURE 7. Attractors for several wave motions expressed by projecting to four two-dimensional subspaces: $x_0 = 0.05$ cm. (*a*) Irregular unidirectionally rotating motion, $T_r = 0.0094$; (*b*) Irregular bidirectionally rotating motion, $T_r = 0.0196$; (*c*) Approximately periodic bidirectionally rotating motion, $T_r = 0.0329$.

this linear part. An example is shown in figure 11. We usually used about 5000 data points.

The ν of the attractors for the irregular bidirectionally rotating motion is 2.1–2.4. This scattering of the values is related to the difference in unevenness of each attractor. The relatively even attractors, as shown in figure 7(*b*), usually give fairly large values (2.3–2.4), while the uneven attractors, as illustrated in figure 8(*c*), give smaller values. In the above results, $R_{\min}$ and $R_{\max}$ were about 0.2 cm and 3.0 cm respectively.

The attractors for the irregular unidirectionally rotating motion give $\nu = 2.0$–2.1 with $R_{\min} \approx 0.1$ cm and $R_{\max} \approx 0.5$ cm. This ν is a little smaller than that for the bidirectionally rotating motion. No reliable value of ν was obtained for the attractor shown in figure 7(*c*) since no linear region of $\log C(R)$ was found.

Next, in order to examine the orbital instability of attractors, the maximum

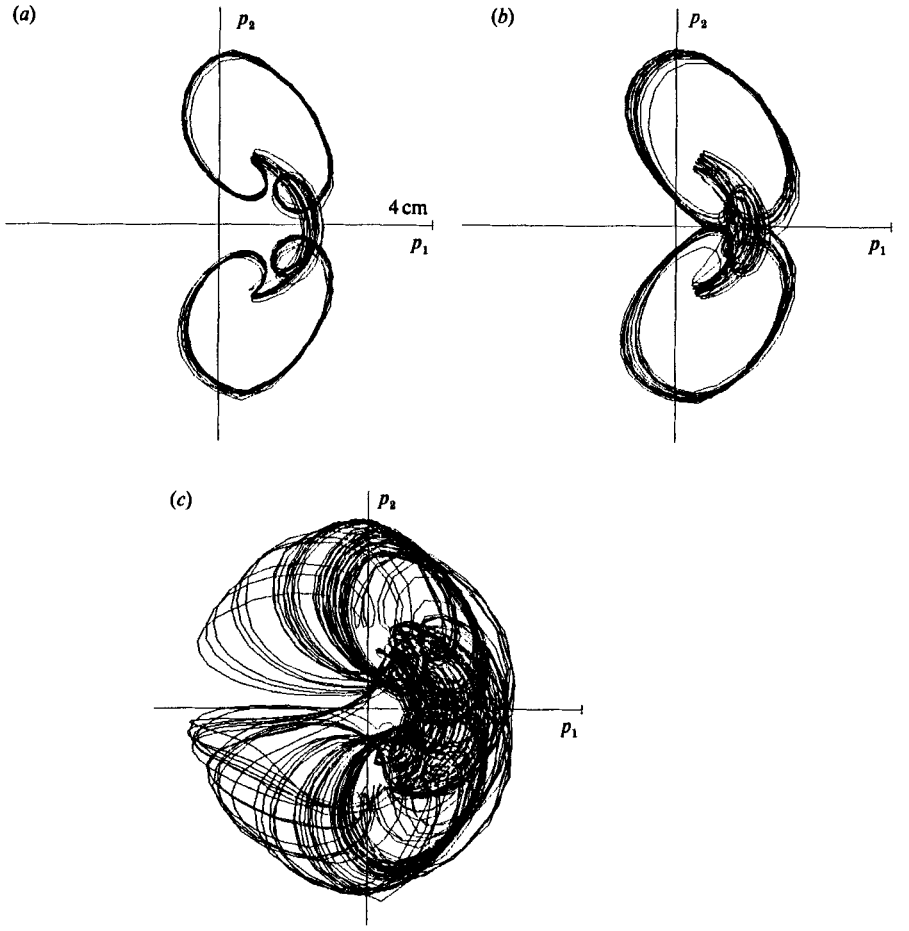

FIGURE 8. (*a*) Trajectory for an unstable approximately periodic wave motion expressed by projecting onto the $(p_1 p_2)$-plane: $x_0 = 0.05$ cm and $T_r = 0.0161$, the orbit during $1100T$ is shown. (*b*) Trajectory for similar motion: $x_0 = 0.05$ cm and $T_r = 0.0192$, the orbit during $1500T$ is shown. (*c*) An example of the uneven attractor for the irregular bidirectionally rotating motion: $x_0 = 0.05$ cm and $T_r = 0.0174$.

Liapunov exponent was computed using the following method with the data given in (3.5). The neighbouring point to $\boldsymbol{p}_1$, $\boldsymbol{p}_{h(1)}$, is chosen so as to satisfy

$$|\boldsymbol{p}_{h(1)} - \boldsymbol{p}_1| \approx \epsilon_m, \tag{3.7}$$

and the neighbouring point to $\boldsymbol{p}_n$, $\boldsymbol{p}_{h(n)}$, is determined so as to satisfy

$$|\boldsymbol{p}_{h(n)} - \boldsymbol{p}_n| \approx \epsilon_m, \tag{3.8}$$

and

$$I_n \equiv \frac{|(\boldsymbol{p}_{h(n)} - \boldsymbol{p}_n, \boldsymbol{p}_{h(n-1)+1} - \boldsymbol{p}_n)|}{|\boldsymbol{p}_{h(n)} - \boldsymbol{p}_n| \cdot |\boldsymbol{p}_{h(n-1)+1} - \boldsymbol{p}_n|} \geqslant S_m, \tag{3.9}$$

for $n = 2, 3, \ldots, N$. Here ϵ_m and S_m are constants. The condition (3.9) is imposed so

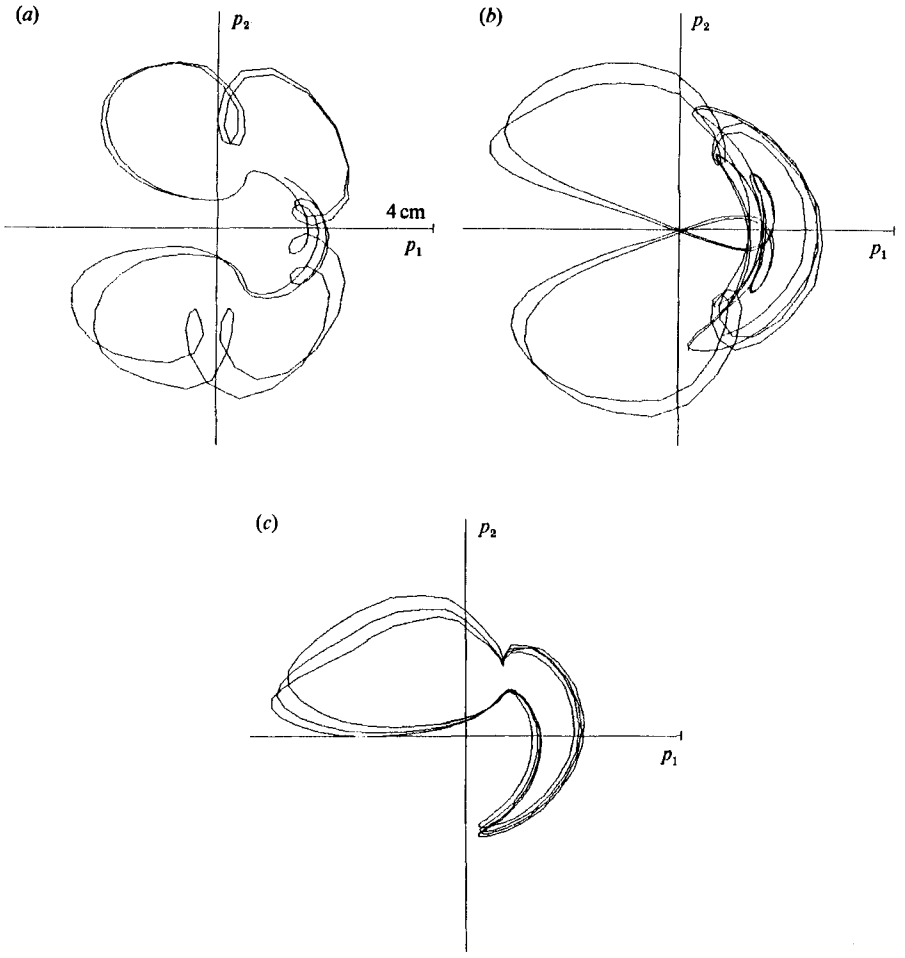

FIGURE 9. Trajectories for unstable approximately periodic wave motions with a small life span expressed by projecting onto the (p_1, p_2)-plane: $x_0 = 0.05$ cm. (*a*) $T_r = 0.0110$, the orbit during $200T$ is shown; (*b*) $T_r = 0.0305$, the orbit during $350T$ is shown; (*c*) $T_r = 0.0229$, the orbit during $240T$ is shown.

that the direction of $\boldsymbol{p}_{h(n)}$ from $\boldsymbol{p}_n$ is near the direction of the largest eigenvalue. Then the maximum Liapunov exponent is computed from

$$\lambda_1 = \frac{1}{N-1} \sum_{n=1}^{N-1} \log \frac{|\boldsymbol{p}_{h(n)+1} - \boldsymbol{p}_{n+1}|}{|\boldsymbol{p}_{h(n)} - \boldsymbol{p}_n|}. \tag{3.10}$$

Since $\boldsymbol{p}_n$ is the datum with time interval T, it can be said that the distance between two neighbouring orbits changes on average as $\exp(\lambda_1 t/T)$. If the ϵ_m chosen is too small, an incorrect value of λ_1 is obtained because of the effect of the noise. Referring to the values of $R_{\min}$ in the computation of ν, we chose ϵ_m as 0.35 cm and 0.12 cm for the attractors expressing the bidirectionally and unidirectionally rotating motions, respectively. The average of I_n was about 0.85 for fixed $S_m = 0.5$.

The attractors for the irregular bidirectionally rotating motion give positive λ_1 between 0.02 and 0.05, which is consistent with their fractional dimension. Attractors with larger unevenness tend to have smaller λ_1 values. But the correlation of λ_1 with

the unevenness is weaker than that of ν. So ν seems more appropriate for discriminating between chaotic attractors of different unevenness.

The attractors for the irregular unidirectionally rotating motion also give positive λ_1. This value is between 0.009 and 0.011 and is smaller than that for the bidirectionally rotating motion.

According to the results described in this subsection, it is concluded that the attractors for the irregular bidirectionally or unidirectionally rotating motion are strange attractors with positive maximum Liapunov exponents and fractional dimensions between 2.0 and 2.4.

4. Evolution equations derived by Miles

Miles (1984*b*) derived evolution equations describing resonantly forced surface waves for the geometrical configuration identical to that of the experiments shown in §§2 and 3. He first assumed the free-surface displacement η as

$$\eta = \kappa\epsilon[(\tilde{p}_1(\tau)\cos\omega t+\tilde{q}_1(\tau)\sin\omega t)\cos\theta+(\tilde{p}_2(\tau)\cos\omega t+\tilde{q}_2(\tau)\sin\omega t)\sin\theta]J_1(kr) +\tilde{N}(r,\theta,t,\tau), \quad (4.1)$$

for the displacement of the forcing oscillation given by (3.1). Here r, θ, ω and k are defined immediately after (3.2). A dimensionless slow time τ is defined by

$$\tau = \tfrac{1}{2}\epsilon^2\omega t, \quad (4.2)$$

where ϵ is a small constant defined as

$$\epsilon = \left(\frac{1.684x_0}{a}\right)^{\frac{1}{3}}. \quad (4.3)$$

The constant κ is given by

$$\kappa = \frac{\tanh kd}{0.3455k}. \quad (4.4)$$

The term $\tilde{N}(r,\theta,t,\tau)$ in (4.1) represents a higher-order term of $O(\epsilon^2)$.

By using the averaged-Lagrangian method, he then derived the following equations describing the slow evolution of p_1, q_1, p_2 and q_2 on assuming that $\epsilon \ll 1$:

$$\left.\begin{aligned}
\frac{\mathrm{d}\tilde{p}_1}{\mathrm{d}\tau} &= -\alpha\tilde{p}_1-(\beta+A\tilde{E})\tilde{q}_1+B\tilde{M}\tilde{p}_2,\\
\frac{\mathrm{d}\tilde{q}_1}{\mathrm{d}\tau} &= -\alpha\tilde{q}_1+(\beta+A\tilde{E})\tilde{p}_1+B\tilde{M}\tilde{q}_2+1,\\
\frac{\mathrm{d}\tilde{p}_2}{\mathrm{d}\tau} &= -\alpha\tilde{p}_2-(\beta+A\tilde{E})\tilde{q}_2-B\tilde{M}\tilde{p}_1,\\
\frac{\mathrm{d}\tilde{q}_2}{\mathrm{d}\tau} &= -\alpha\tilde{q}_2+(\beta+A\tilde{E})\tilde{p}_2-B\tilde{M}\tilde{q}_1.
\end{aligned}\right\} \quad (4.5)$$

Here he assumed linear damping with constant α. Also $\tilde{E}$ and $\tilde{M}$, defined by

$$\left.\begin{aligned}
\tilde{E} &= \tfrac{1}{2}(\tilde{p}_1^2+\tilde{q}_1^2+\tilde{p}_2^2+\tilde{q}_2^2),\\
\tilde{M} &= \tilde{p}_1\tilde{q}_2-\tilde{p}_2\tilde{q}_1,
\end{aligned}\right\} \quad (4.6)$$

are measures of the energy and the angular momentum in the modes given in (1.1).

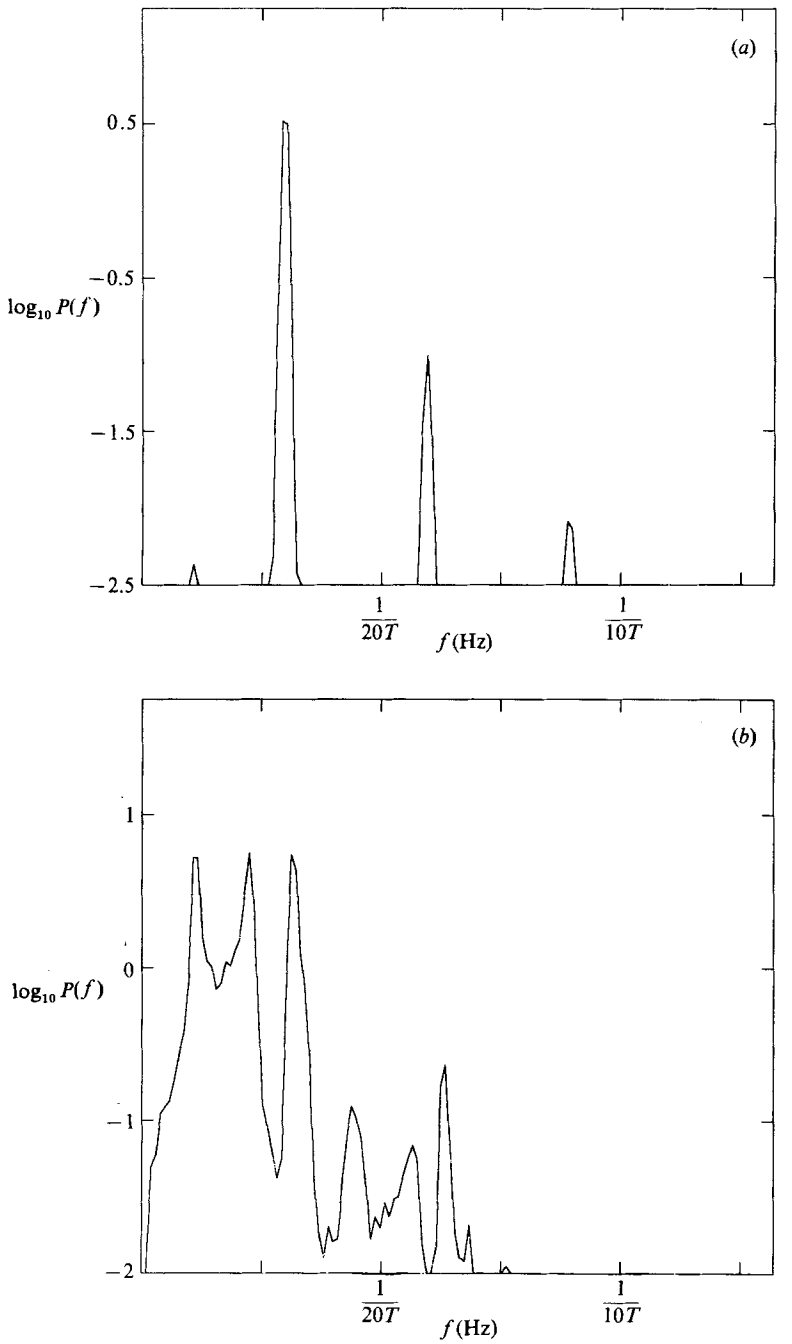

FIGURE 10(*a*, *b*). For caption see facing page.

Both A and B are constants that depend only on d/a. (The method for their computation is introduced in Miles 1984*b*). The value β is the frequency offset defined by

$$\beta = \frac{\omega^2 - \omega_0^2}{\epsilon^2 \omega_0^2}, \tag{4.7}$$

where $\omega_0 = 2\pi/T_0$. The assumption of a small ϵ means that the displacement of

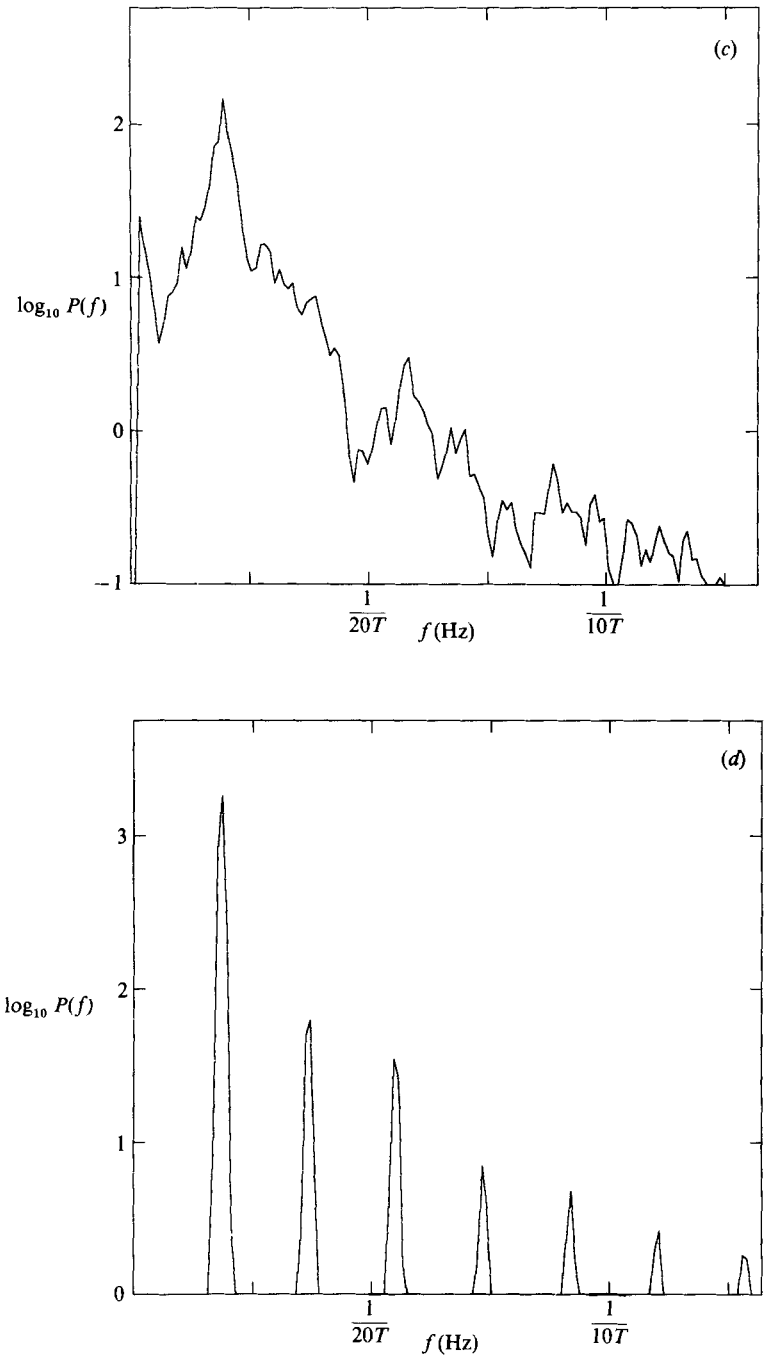

FIGURE 10. Power spectra shown on a logarithmic scale computed from the evolution of E: $x_0 = 0.05$ cm. (*a*) $T_r = 0.0076$; (*b*) 0.0094; (*c*) 0.0196; (*d*) 0.0329.

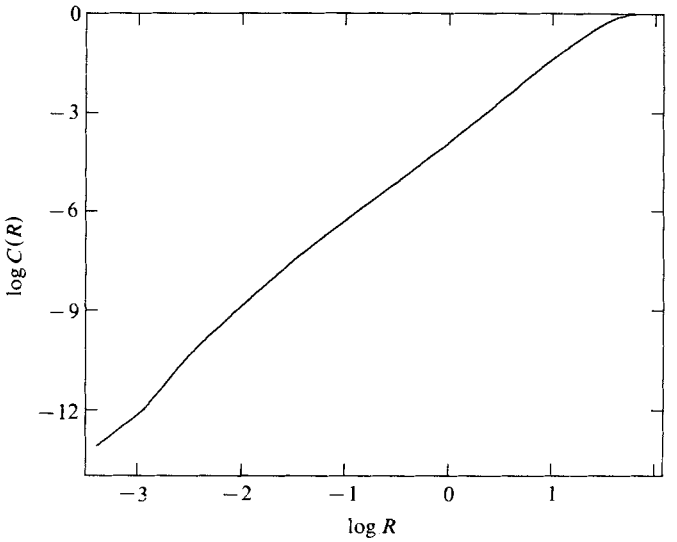

FIGURE 11. The correlation function $C(R)$ for $x_0 = 0.05$ cm and $T_r = 0.0196$. The number of data points $N = 4800$.

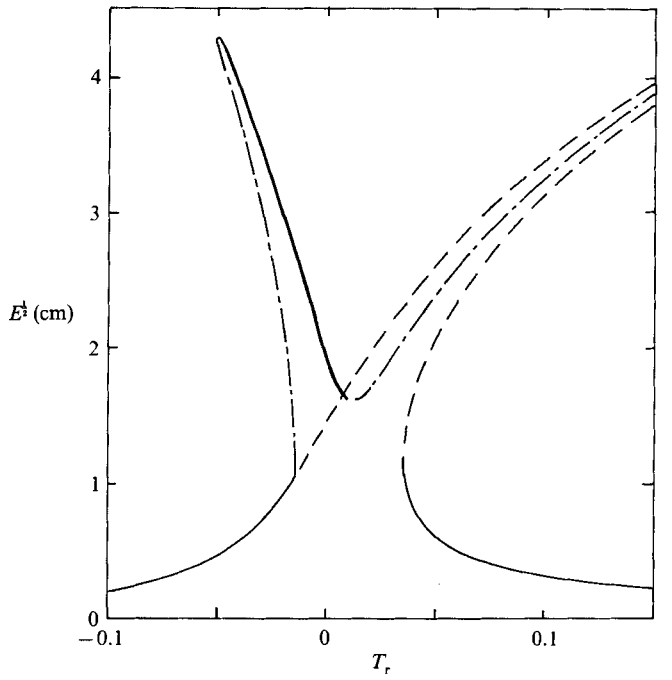

FIGURE 12. The relation between T_r and $E^{\frac{1}{2}}$ associated with two kinds of fixed points of (4.5): $x_0 = 0.05$ cm. Thin solid lines and broken lines denote stable and unstable fixed points corresponding to the regular planar oscillation. A bold solid line and dotted broken lines denote stable and unstable fixed points corresponding to the regular rotational motion.

FIGURE 13. Chaotic regions and many narrow windows for limit cycles computed from the solutions to (4.5). For each T_r the set of values taken by M when p_1 yields its average value is shown. $x_0 = 0.05$ cm.

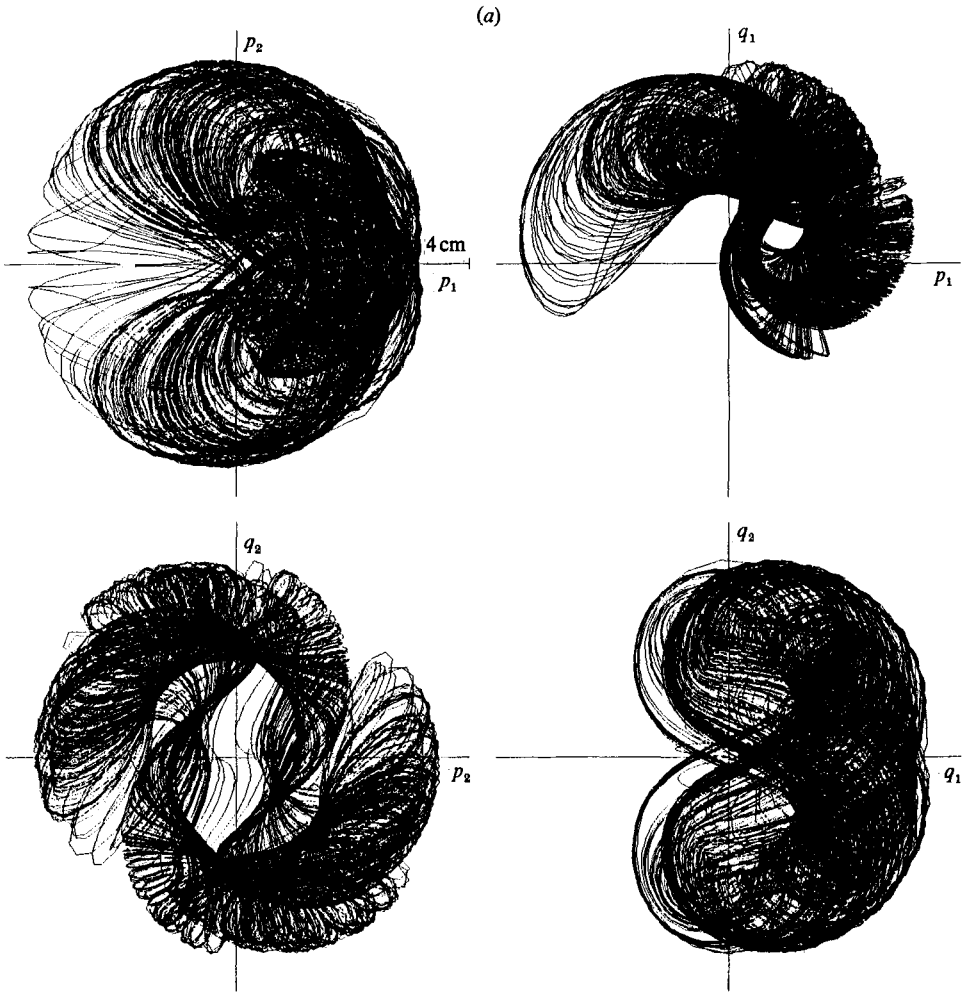

FIGURE 14(*a*). For caption see facing page.

the forcing oscillation is sufficiently small that the free-surface displacement is also small, and that the frequency offset is sufficiently small that the evolution of $\tilde{\boldsymbol{p}} = (\tilde{p}_1, \tilde{q}_1, \tilde{p}_2, \tilde{q}_2)$ is slow.

Hereinafter we fix the values of A and B at

$$A = 1.09, \quad B = -1.49, \tag{4.8}$$

which correspond to $a = 9.24$ cm and $d = 14.1$ cm, used in the experiments.

The value of α was determined from the experimental data using the following method. First we produced some regular rotational motions or regular planar oscillations by oscillating with appropriate values of (ω, x_0). After the sudden end of the oscillation, we observed the damping of the free-surface displacements at one or two measuring points. Under the assumption that the amplitudes decrease as

$$\eta \propto \exp(-\delta\omega t), \tag{4.9}$$

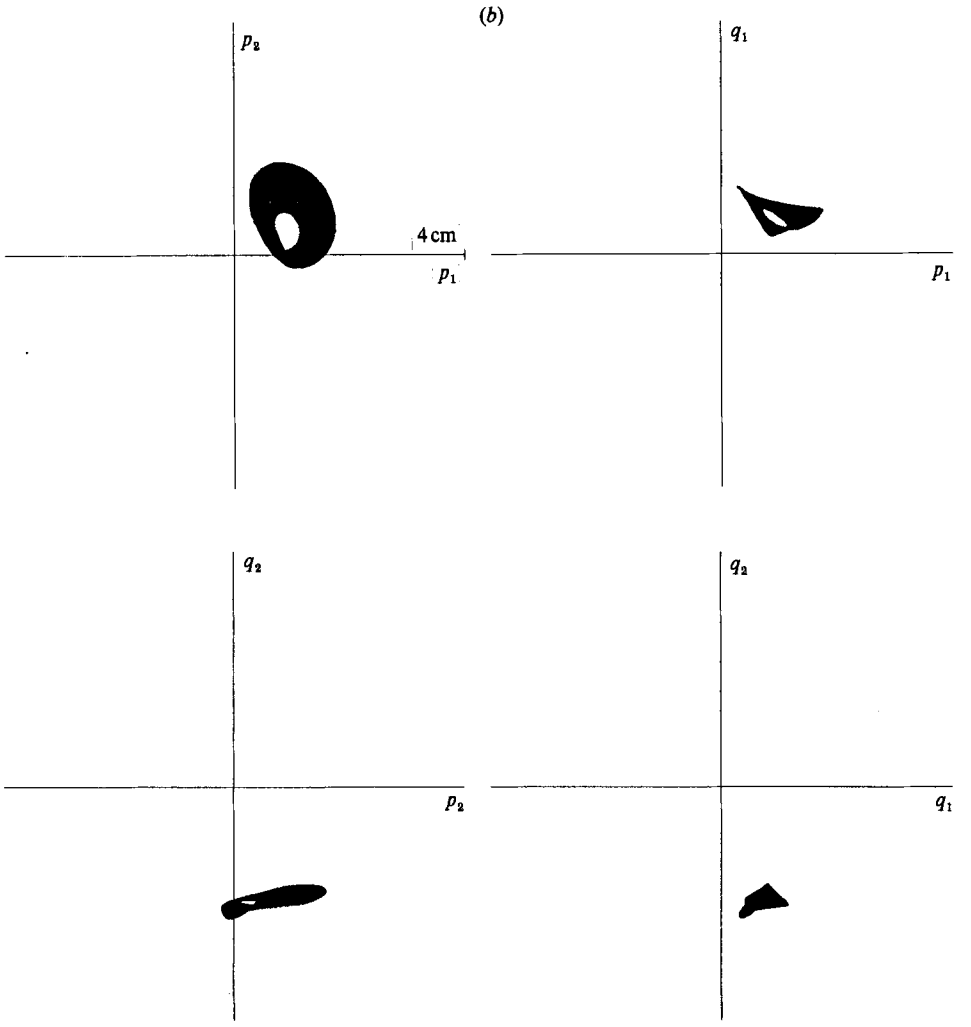

FIGURE 14. Chaotic attractors of (4.5) expressed by projecting onto four two-dimensional subspaces: $x_0 = 0.05$ cm. (*a*) Bidirectional chaotic attractor, $T_r = 0.02160$; (*b*) unidirectional chaotic attractor, $T_r = 0.01077$.

we obtained $\delta \sim 0.0043$ in the experimental configuration, although a little scattering of values was observed. δ and α are related by

$$\alpha = \frac{2\delta}{\epsilon^2}. \tag{4.10}$$

There is no evidence supporting the assumption of linear damping with constant ratio. In particular, the applicability of this assumption is doubtful when the amplitude of the wave motion changes irregularly or periodically. In spite of this problem, we adopt this assumption as the first step in our examination and use the value of α computed by (4.10).

Hereinafter, we show the results of computations using the variables defined in §§2

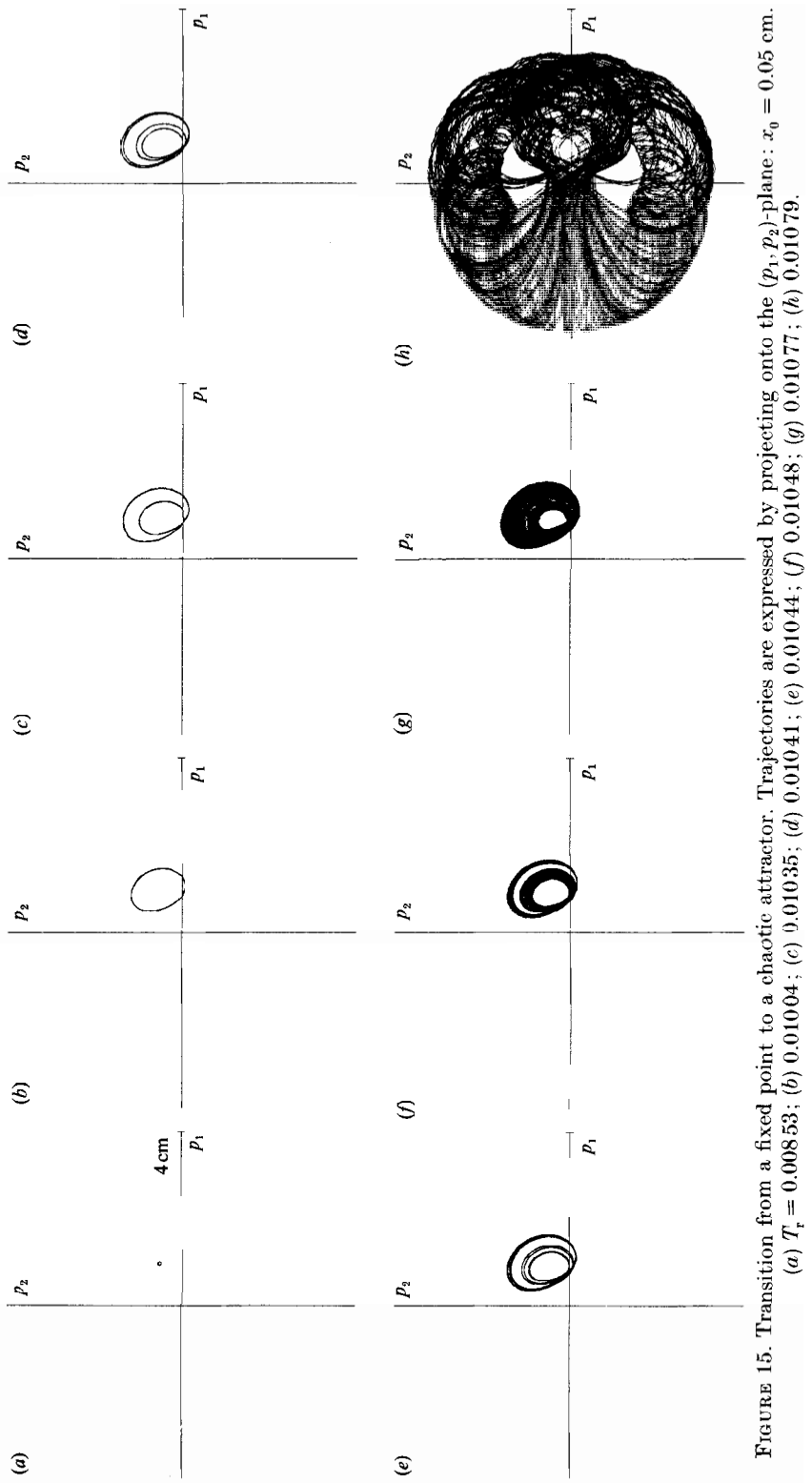

FIGURE 15. Transition from a fixed point to a chaotic attractor. Trajectories are expressed by projecting onto the (p_1, p_2)-plane: $x_0 = 0.05$ cm. (*a*) $T_r = 0.00853$; (*b*) 0.01004; (*c*) 0.01035; (*d*) 0.01041; (*e*) 0.01044; (*f*) 0.01048; (*g*) 0.01077; (*h*) 0.01079.

and 3, in order to facilitate direct comparisons with the experimental results. The relations between these variables and those defined in (4.1) and (4.6) are given by

$$\left.\begin{aligned} p_n &= s\tilde{p}_n, \quad q_n = s\tilde{q}_n \quad (n = 1, 2), \\ E &= s^2\tilde{E}, \quad M = p_1 q_2 - p_2 q_1 = s^2\tilde{M}, \end{aligned}\right\} \tag{4.11}$$

where s is defined by

$$s = \kappa\epsilon J_1(0.87ak). \tag{4.12}$$

Also, T_r is used in place of ω.

The fixed points of (4.5) and their stability were examined in detail by Miles (1984*b*, *c*). There are two kinds of fixed points. The first, which he called planar harmonic, expresses the regular planar oscillation. The second, called non-planar harmonic, expresses the regular rotational motion. The relation between T_r and $E^{\frac{1}{2}}$ associated with these fixed points is shown in figure 12 for $x_0 = 0.05$ cm. Thin solid lines show that, for T_r larger than a certain positive value or smaller than a certain negative value, the regular planar oscillation exists stably. The bold line shows that, for T_r between certain positive and negative values, the regular rotational motion exists stably. Moreover, there is a certain range where both these motions are stable. On the other hand, for T_r between certain two positive values ($0.00852 < T_r < 0.03501$), no stable fixed point exists. Similar results are obtained for other x_0 satisfying $0.016 \text{ cm} \leqslant x_0 \leqslant 0.1$ cm, as shown in figure 2. Here broken lines denote the above boundary values.

In order to examine the asymptotic behaviour of the solution to (4.5) in the region with no stable fixed point (the region between L_3' and L_4' in figure 2), we carried out numerical integration with double precision. Here we used an Adams routine in which the time increments and the degrees of interpolation polynomials used in computing predictors and correctors are determined so that relative error is less than 10^{-14}. The results are shown in the next section.

5. Chaotic attractors and limit cycles of (4.5)

The results of a systematic survey of asymptotic solutions to (4.5) within and near the parametric region with no stable fixed point are given in this section. Here the parameters in (4.5) were chosen so that $x_0 = 0.05$ cm and $0.00831 \leqslant T_r \leqslant 0.03556$. We usually regard the solutions during the time $3000T \leqslant t \leqslant 11000T$ as asymptotic ones.

In order to examine the dependence of the characteristics of the asymptotic solutions on T_r, we extract the following data from each solution. That is, first the average value of p_1, $\langle p_1 \rangle$, is computed. Then we obtain the set of values taken by M when the orbit of the solution intersects the hyperplane $p_1 = \langle p_1 \rangle$. If the trajectory of the solution is a periodic orbit, the set contains only a few points. On the other hand, if the trajectory behaves chaotically, an infinite number of points will be contained in the set. Figure 13 shows this set computed for each T_r. Here the value of $\boldsymbol{p} = (p_1, q_1, p_2, q_2)$ at the final time in the numerical integration with a slightly smaller T_r was used as the initial value for each T_r. Chaotic attractors are observed in wide ranges of T_r, while many narrow windows for limit cycles are also found. These alternate appearances of chaotic attractors and limit cycles have already been found by Miles (1984*b*, *c*). No regularity is found for the position or the width of the windows.

A typical chaotic attractor is shown in figure 14 (*a*). The attractors most commonly

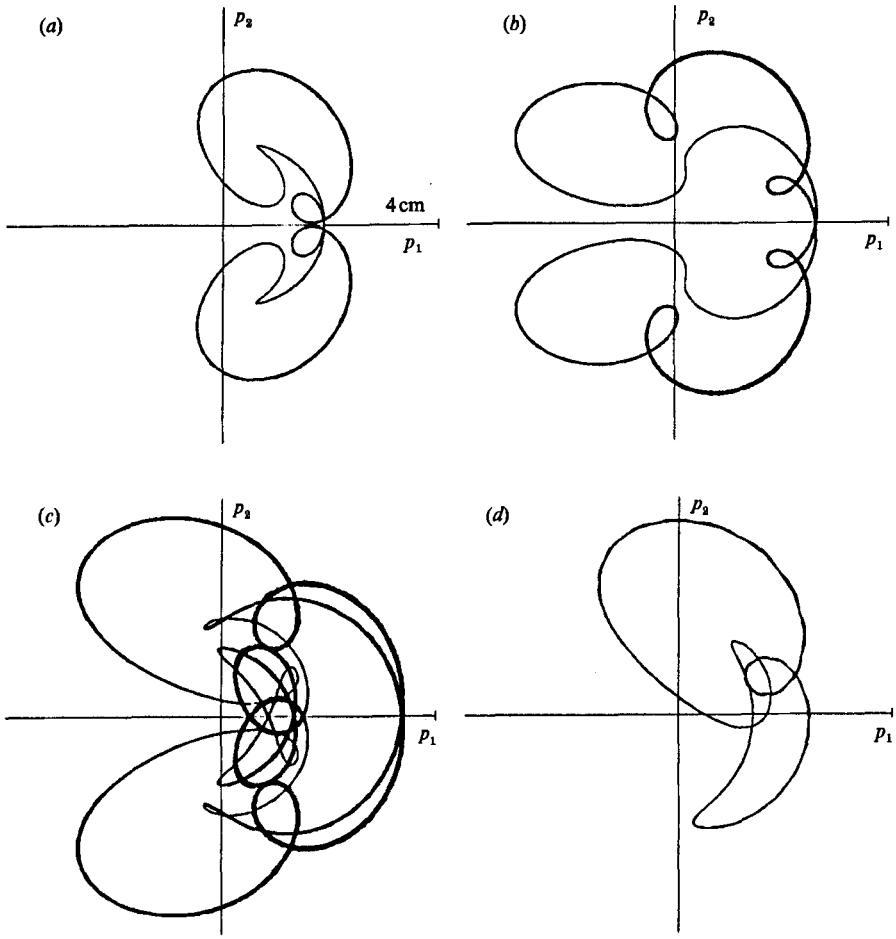

FIGURE 16. A few limit cycles of (4.5) expressed by projecting onto the (p_1, p_2)-plane: $x_0 = 0.05$ cm. (*a*) $T_r = 0.01823$; (*b*) 0.01540; (*c*) 0.03246; (*d*) 0.02969.

observed are similar to this. Since M, a measure of the rotation of waves, can yield both positive and negative values for this type of attractor, we call it a bidirectional chaotic attractor.

Next we examine some bifurcations and the transitions between chaotic attractors of different type. When T_r increases from the value corresponding to stable fixed points, the route to chaos associated with the Hopf bifurcation and successive period-doubling bifurcations is observed, as shown in figure 15(*a–g*). (These bifurcations have already been found by Miles 1984*b*, *c*.) We call the attractor shown in figures 15(*g*) or 14 (*b*) a unidirectional chaotic attractor, because M yields positive or negative definite values for it. The transition between the unidirectional and bidirectional chaotic attractors is observed at $T_r = 0.01078$, as shown in figure 15(*g*, *h*). When this transition occurs, the wave energy increases greatly.

The largest window for limit cycles is observed for T_r around 0.0187. A typical limit cycle found in this window is shown in figure 16(*a*). Some other limit cycles observed in other windows are shown in figure 16(*b–d*).

Next, in order to characterize quantitatively a few kinds of attractors introduced in this section, the correlation dimension ν and the maximum Liapunov exponent

were computed. The value of ν is computed from the correlation function $C(R)$ using the method shown in §3.4. We used at least 10000–34000 data points.

Most of the bidirectional chaotic attractors yield values of ν between 2.1 and 2.4. It seems that this scattering of ν reflects the difference in the unevenness of the trajectory of each attractor. Attractors with larger unevenness tend to have smaller values of ν. On the other hand, the unidirectional chaotic attractors give values of ν between 1.95 and 2.05. For the limit cycles, of course, ν is very close to 1.

Next we calculate the maximum Liapunov exponent using the following method. We first compute the asymptotic solution

$$\boldsymbol{p}_n = (p_1(nT), q_1(nT), p_2(nT), q_2(nT)) \quad (n = 1, 2, \ldots, N) \tag{5.1}$$

by the numerical integration of (4.5). The neighbouring point to $\boldsymbol{p}_1$, $\boldsymbol{p}_1^*$, is chosen so as to satisfy

$$|\boldsymbol{p}_1^* - \boldsymbol{p}_1| = \epsilon_m, \tag{5.2}$$

and

$$(\boldsymbol{p}_1^* - \boldsymbol{p}_1, \boldsymbol{p}_2 - \boldsymbol{p}_1) = 0, \tag{5.3}$$

and the neighbouring point to $\boldsymbol{p}_n$, $\boldsymbol{p}_n^*$, is determined by the formula

$$\boldsymbol{p}_n^* = \boldsymbol{p}_n + \frac{\epsilon_m}{|\boldsymbol{p}_n' - \boldsymbol{p}_n|}(\boldsymbol{p}_n' - \boldsymbol{p}_n), \quad \text{for } n = 2, 3, \ldots, N. \tag{5.4}$$

Here ϵ_m is a constant and $\boldsymbol{p}_n'$ is the value of $\boldsymbol{p}$ obtained by the numerical integration of (4.5) over the time $t = T$ with the initial value $\boldsymbol{p}_{n-1}^*$. Then the maximum Liapunov exponent is computed from

$$\lambda_1 = \frac{1}{N-1} \sum_{n=1}^{N-1} \log \frac{|\boldsymbol{p}_{n+1}' - \boldsymbol{p}_{n+1}|}{|\boldsymbol{p}_n^* - \boldsymbol{p}_n|}. \tag{5.5}$$

Since $\boldsymbol{p}_n$ is the datum with time interval T it can be said that the distance between two neighbouring orbits changes on average as $\exp(\lambda_1 t/T)$. We chose ϵ_m as 10^{-6} and N as 8000.

It is found that the chaotic attractors certainly have positive maximum Liapunov exponents. The bidirectional chaotic attractors give $\lambda_1 = 0.018$–0.032, while the unidirectional ones give smaller values: $\lambda_1 = 0.012$–0.013. Furthermore, as in the case of ν, attractors with larger unevenness tend to have smaller λ_1 values.

6. Comparison between theoretical and experimental results

In this section the behaviour of asymptotic solutions to (4.5) described in §§4 and 5 is compared with the experimental results given in §3.

The phase diagram is shown in figure 2. The parametric regions where the regular planar oscillations and/or the regular rotational motions can be experimentally observed almost coincide with the regions where the stable fixed points corresponding to those wave motions exist, although some discrepancy is found between L_1 and L_1' for relatively large x_0 (The reason for this discrepancy will be discussed below.) Furthermore, the region where periodic or irregular wave motions are observed (between L_3 and L_4) also corresponds to the region, between L_3' and L_4', where limit cycles or chaotic attractors are found as the solutions to (4.5).

Hereinafter a detailed comparison is made only for $x_0 = 0.05$ cm. Figure 5 shows the values of $(p_1^2 + q_1^2)^{\frac{1}{2}}$ for the two regular wave motions. The experimental values for the regular planar oscillation, denoted by circles, agree fairly well with the corresponding theoretical values expressed by thin solid lines. For the regular

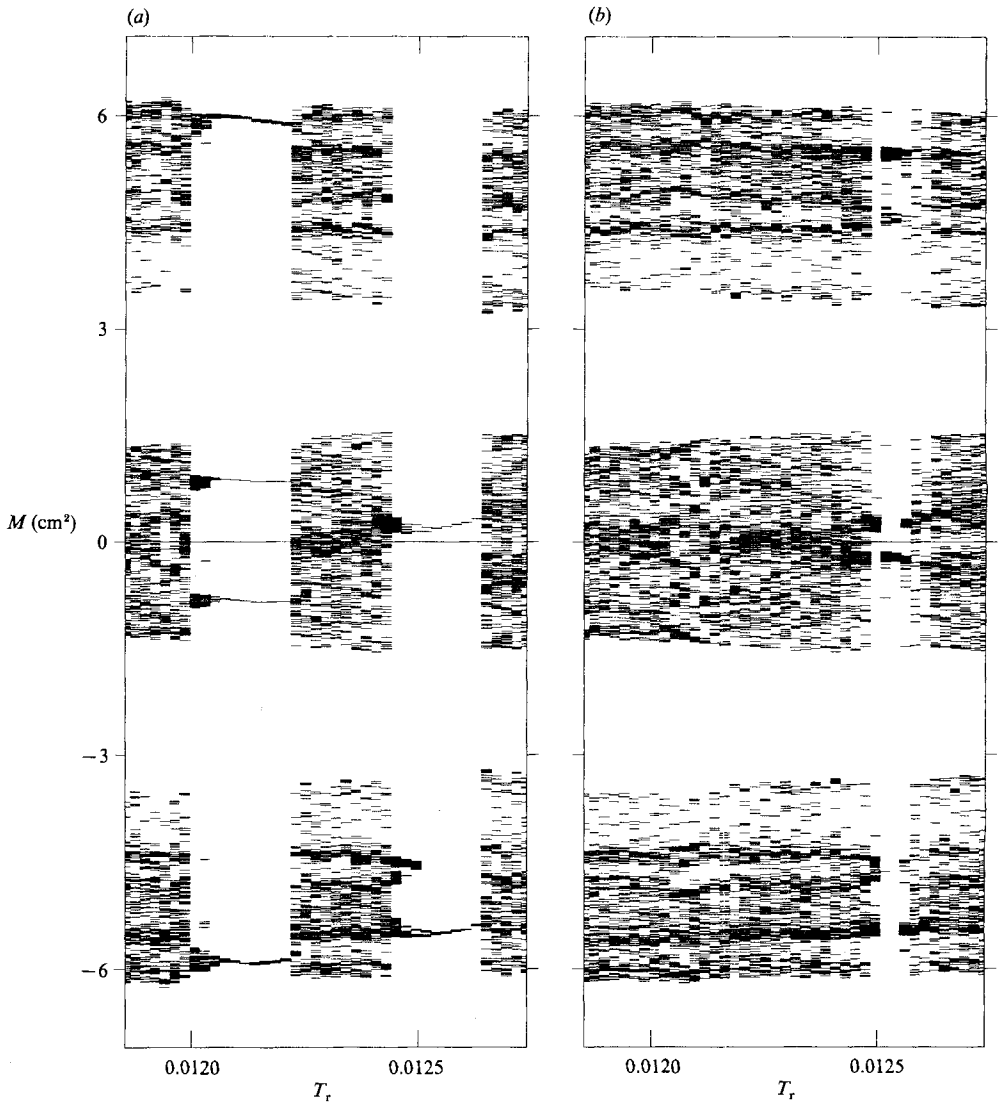

FIGURE 17. The dependence of the asymptotic solutions to (4.5) on the variation of the oscillation period T in the case of small windows. For each T_r the set of values taken by M when p_1 yields its average value is shown: $x_0 = 0.05$ cm. (*a*) Without variation of T; (*b*) with variation of T.

rotational motion, the agreement between experimental values, denoted by crosses, and the theoretical ones, denoted by a bold solid line, is a little poor for relatively large $(p_1^2+q_1^2)^{\frac{1}{2}}$. This discrepancy seems due to the strong nonlinearity neglected in the theory, because the ratio of the wave amplitude to the radius of the container reaches 0.3–0.4 in the experiments.

Next we compare the chaotic attractors that are commonly found both in the experiments and in the theory, and correspond to the irregular bidirectionally rotating motion. Their shapes, shown in figures 7(*b*) and 14(*a*), are very similar. Moreover, there is fairly good agreement between the values of ν and λ_1 for the experimental attractors and the numerically determined ones. That is, $\nu = 2.1$–2.4

and $\lambda_1 = 0.02$–0.05 for the experimental ones, and $\nu = 2.1$–2.4 and $\lambda_1 = 0.018$–0.032 for the numerical ones. Furthermore, both in the experiments and in the theory, we find that attractors with larger unevenness tend to have smaller ν and λ_1 values.

The second chaotic attractor found in the experiments, which corresponds to the irregular unidirectionally rotating motion and is shown in figure 7 (*a*), is similar to the unidirectional chaotic attractor shown in figure 14 (*b*). The former gives $\nu = 2.0$–2.1 and $\lambda_1 = 0.009$–0.011, while the latter gives $\nu = 1.95$–2.05 and $\lambda_1 = 0.012$–0.013.

The experimental attractor shown in figure 7 (*c*), which expresses the approximately periodic bidirectionally rotating motion, has no direct correspondent in the theory, although there is a little similarity between this and the limit cycle shown in figure 16 (*d*). This attractor is observed in the parametric region close to that of the regular planar oscillation. However, in this region we could find no evidence in the theory of the existence of a relatively large window for a limit cycle.

In contrast, many of the limit cycles found in the theory were not observed in the experiments. One exception is a series of attractors corresponding to periodic or irregular unidirectionally rotating motions shown in figures 6 and 7 (*a*). Consistently with the theory, the route to chaos associated with a period-doubling bifurcation is observed, although only one bifurcation could be confirmed. In the experiments, we also found some unstable approximately periodic wave motions. Some of them, shown in figure 8 (*a*, *b*), are very similar to the limit cycle shown in figure 16 (*a*). Other examples of this kind, of lesser similarity, are found between figures 9 (*a*–*c*) and 16 (*b*–*d*).

Because of the above failure in observing long-lived periodic wave motions, it is suggested that the unavoidable variation of the forcing period T is too large to allow these motions. This seems correct with respect to small windows, because the amount of the variation of T is certainly considerably larger than their width. In order to confirm this, we made a numerical integration of (4.5) with an allowance for the variation of T. That is, the value of β in (4.5) was varied randomly at every time interval $t = T$ so that the corresponding variation of T has a Gaussian distribution of standard deviation of 0.00005 s, which represents the variation in the experiments and corresponds to 0.00011 of T_r. The results for the quantities defined in figure 13 are shown in figure 17. The two small windows found in figure 17 (*a*) for no variation of T almost break down in figure 17 (*b*) for the above variation of T.

However, there are also some relatively large windows whose width is considerably larger than, or comparable with, the amount of the variation of T in the experiments. A comparison similar to figure 17 was made for the largest window around $T_r = 0.0187$ and, as shown in figure 18, most of the limit cycles essentially retain their identities. The discrepancy between this result and the failure in observing long-lived periodic wave motions in this parametric region suggests that the validity of the assumptions of weak nonlinearity and linear constant damping in the theory should be assessed. The ϵ defined in (4.3) should be small according to the theory, while $\epsilon = 0.21$ in the experiments with $x_0 = 0.05$ cm. This value is not particularly small. Furthermore, for surface waves of not particularly small amplitude, it seems more reasonable to assume a nonlinear damping. Therefore, a more accurate theory may also be required in order to resolve completely the problem of the discrepancies between the experiments and the theory.

In spite of some discrepancies, mentioned above, it can be concluded that the weakly nonlinear equations (4.5) explain well most of the evolution of surface waves even for the irregular motions. This is a little surprising considering the large wave amplitude in the experiments.

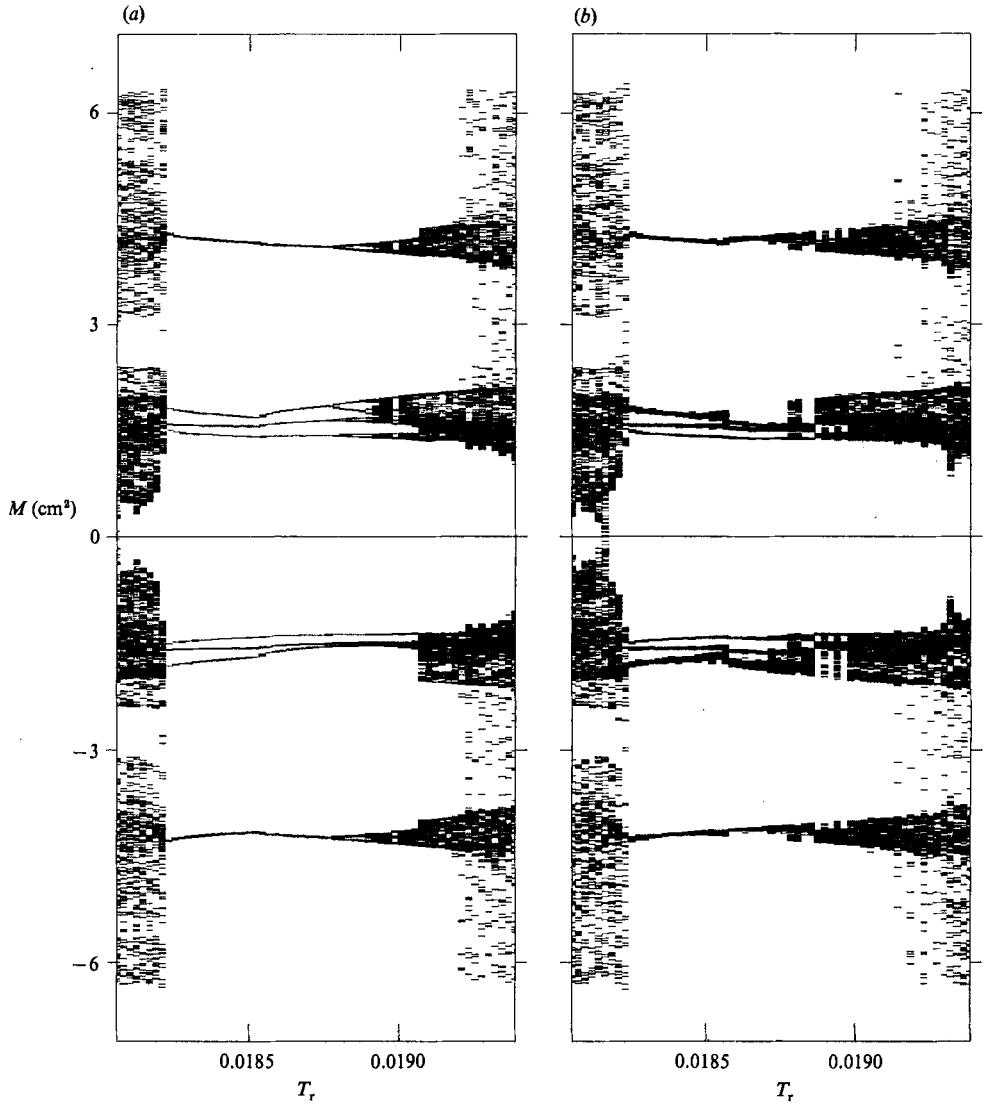

FIGURE 18. The dependence of the asymptotic solutions to (4.5) on the variation of the oscillation period T, as in figure 17 but for the case of a large window. $x_0 = 0.05$ cm. (*a*) Without variation of T; (*b*) with variation of T.

7. The relevance to the experiments by Ciliberto & Gollub

Some of the characteristics of the irregular motion in our experiments are similar to those of Ciliberto & Gollub (1985). Thus it seems interesting to compare the two experiments in detail.

Their experiments are similar to ours in that at most two modes are excited by the oscillation. (Although four modes could be excited in their experiments only two modes were, perhaps because of small unavoidable asymmetries in the geometrical configuration.) There are, however, some differences between our and their experimental configurations. First, whereas only one of the relevant modes is excited directly by horizontal oscillation in our experiments, in theirs both relevant modes

are excited parametrically by vertical oscillation at frequencies close to double the natural ones. Secondly, while our natural frequencies of the relevant modes are strictly equal, their frequencies differ from each other by small amounts. Thirdly, they used a cylindrical fluid layer of depth $d = 1$ cm in a container of radius $a = 6.35$ cm. Therefore, the excited waves must be regarded as shallow-water capillary–gravity waves in contrast with the waves in our experiments with $a = 9.24$ cm and $d = 14.1$ cm.

Because of the small variations in natural frequencies in their experiment, we cannot make a direct comparison for the regions where irregular surface waves are observed. But some of the characteristics of the attractors in these regions are similar. That is, the chaotic attractor examined by them has a correlation dimension close to 2.2 and has a positive maximum Liapunov exponent. This result is similar to ours for the most common chaotic attractor, although its correlation dimension is scattered in the range of 2.1–2.4. (Here note that, unlike us, they used the method of reconstruction of the attractors in a phase space. But this does not seem to give rise to serious problems in comparing, because they suggest that four variables are sufficient to describe their irregular motions.) Furthermore, the route to chaos associated with period-doubling bifurcation is observed in both experiments.

In view of the above results, it would be interesting to study whether results similar to ours can be obtained for other systems where only two modes are relevant. Furthermore, it may also be valuable to examine systems where at least three modes are relevant.

We wish to thank Professor M. Oikawa for his continual encouragement. We acknowledge the technical assistance of Miss S. Hoshino.

REFERENCES

CILIBERTO, S. & GOLLUB, J. P. 1985 Chaotic mode competition in parametrically forced surface waves. *J. Fluid Mech.* **158**, 381–398.

GOLLUB, J. P. & MEYER, C. W. 1983 Symmetry-breaking instabilities on a fluid surface. *Physica* **6D**, 337–346.

GRASSBERGER, P. & PROCACCIA, I. 1983 Characterization of strange attractors. *Phys. Rev. Lett.* **50**, 346–349.

HUTTON, R. E. 1963 An investigation of resonant, nonlinear, nonplanar free surface oscillations of a fluid. *NASA Tech. Note* D-1870 (Washington).

KEOLIAN, R., TURKEVICH, L. A., PUTTERMAN, S. J., RUDNICK, I. & RUDNICK, J. A. 1981 Subharmonic sequences in the Faraday experiment: departures from period doubling. *Phys. Rev. Lett.* **47**, 1133–1136.

MILES, J. W. 1976 Nonlinear surface waves in closed basins. *J. Fluid Mech.* **75**, 419–448.

MILES, J. W. 1984*a* Nonlinear Faraday resonance. *J. Fluid Mech.* **146**, 285–302.

MILES, J. W. 1984*b* Resonantly forced surface waves in a circular cylinder. *J. Fluid Mech.* **149**, 15–31.

MILES, J. W. 1984*c* Resonant motion of a spherical pendulum. *Physica* **11D**, 309–323.